

Observation of $e^+e^- \rightarrow \eta' J/\psi$ at center-of-mass energies between 4.189 and 4.600 GeV

M. Ablikim¹, M. N. Achasov^{9,e}, S. Ahmed¹⁴, X. C. Ai¹, O. Albayrak⁵, M. Albrecht⁴, D. J. Ambrose⁴⁴, A. Amoroso^{49A,49C}, F. F. An¹, Q. An^{46,a}, J. Z. Bai¹, R. Baldini Ferroli^{20A}, Y. Ban³¹, D. W. Bennett¹⁹, J. V. Bennett⁵, N. Berger²², M. Bertani^{20A}, D. Bettoni^{21A}, J. M. Bian⁴³, F. Bianchi^{49A,49C}, E. Boger^{23,c}, I. Boyko²³, R. A. Briere⁵, H. Cai⁵¹, X. Cai^{1,a}, O. Cakir^{40A}, A. Calcaterra^{20A}, G. F. Cao¹, S. A. Cetin^{40B}, J. F. Chang^{1,a}, G. Chelkov^{23,c,d}, G. Chen¹, H. S. Chen¹, H. Y. Chen², J. C. Chen¹, M. L. Chen^{1,a}, S. Chen⁴¹, S. J. Chen²⁹, X. Chen^{1,a}, X. R. Chen²⁶, Y. B. Chen^{1,a}, H. P. Cheng¹⁷, X. K. Chu³¹, G. Cibinetto^{21A}, H. L. Dai^{1,a}, J. P. Dai³⁴, A. Dbeyssi¹⁴, D. Dedovich²³, Z. Y. Deng¹, A. Denig²², I. Denysenko²³, M. Destefanis^{49A,49C}, F. De Mori^{49A,49C}, Y. Ding²⁷, C. Dong³⁰, J. Dong^{1,a}, L. Y. Dong¹, M. Y. Dong^{1,a}, Z. L. Dou²⁹, S. X. Du⁵³, P. F. Duan¹, J. Z. Fan³⁹, J. Fang^{1,a}, S. S. Fang¹, X. Fang^{46,a}, Y. Fang¹, R. Farinelli^{21A,21B}, L. Fava^{49B,49C}, O. Fedorov²³, F. Feldbauer²², G. Felici^{20A}, C. Q. Feng^{46,a}, E. Fioravanti^{21A}, M. Fritsch^{14,22}, C. D. Fu¹, Q. Gao¹, X. L. Gao^{46,a}, X. Y. Gao², Y. Gao³⁹, Z. Gao^{46,a}, I. Garzia^{21A}, K. Goetzen¹⁰, L. Gong³⁰, W. X. Gong^{1,a}, W. Gradl²², M. Greco^{49A,49C}, M. H. Gu^{1,a}, Y. T. Gu¹², Y. H. Guan¹, A. Q. Guo¹, L. B. Guo²⁸, R. P. Guo¹, Y. Guo¹, Y. P. Guo²², Z. Haddadi²⁵, A. Hafner²², S. Han⁵¹, X. Q. Hao¹⁵, F. A. Harris⁴², K. L. He¹, F. H. Heinsius⁴, T. Held⁴, Y. K. Heng^{1,a}, T. Holtmann⁴, Z. L. Hou¹, C. Hu²⁸, H. M. Hu¹, J. F. Hu^{49A,49C}, T. Hu^{1,a}, Y. Hu¹, G. S. Huang^{46,a}, J. S. Huang¹⁵, X. T. Huang³³, X. Z. Huang²⁹, Y. Huang²⁹, Z. L. Huang²⁷, T. Hussain⁴⁸, Q. Ji¹, Q. P. Ji³⁰, X. B. Ji¹, X. L. Ji^{1,a}, L. W. Jiang⁵¹, X. S. Jiang^{1,a}, X. Y. Jiang³⁰, J. B. Jiao³³, Z. Jiao¹⁷, D. P. Jin^{1,a}, S. Jin¹, T. Johansson⁵⁰, A. Julin⁴³, N. Kalantar-Nayestanaki²⁵, X. L. Kang¹, X. S. Kang³⁰, M. Kavatsyuk²⁵, B. C. Ke⁵, P. Kiese²², R. Kliemt¹⁴, B. Kloss²², O. B. Kolcu^{40B,h}, B. Kopf⁴, M. Kornicer⁴², A. Kupsc⁵⁰, W. Kühn²⁴, J. S. Lange²⁴, M. Lara¹⁹, P. Larin¹⁴, H. Leithoff²², C. Leng^{49C}, C. Li⁵⁰, Cheng Li^{46,a}, D. M. Li⁵³, F. Li^{1,a}, F. Y. Li³¹, G. Li¹, H. B. Li¹, H. J. Li¹, J. C. Li¹, Jin Li³², K. Li³³, K. Li¹³, Lei Li³, P. R. Li⁴¹, Q. Y. Li³³, T. Li³³, W. D. Li¹, W. G. Li¹, X. L. Li³³, X. N. Li^{1,a}, X. Q. Li³⁰, Y. B. Li², Z. B. Li³⁸, H. Liang^{46,a}, Y. F. Liang³⁶, Y. T. Liang²⁴, G. R. Liao¹¹, D. X. Lin¹⁴, B. Liu³⁴, B. J. Liu¹, C. X. Liu¹, D. Liu^{46,a}, F. H. Liu³⁵, Fang Liu¹, Feng Liu⁶, H. B. Liu¹², H. H. Liu¹⁶, H. H. Liu¹, H. M. Liu¹, J. Liu¹, J. B. Liu^{46,a}, J. P. Liu⁵¹, J. Y. Liu¹, K. Liu³⁹, K. Y. Liu²⁷, L. D. Liu³¹, P. L. Liu^{1,a}, Q. Liu⁴¹, S. B. Liu^{46,a}, X. Liu²⁶, Y. B. Liu³⁰, Y. Y. Liu³⁰, Z. A. Liu^{1,a}, Zhiqing Liu²², H. Loehner²⁵, X. C. Lou^{1,a,g}, H. J. Lu¹⁷, J. G. Lu^{1,a}, Y. Lu¹, Y. P. Lu^{1,a}, C. L. Luo²⁸, M. X. Luo⁵², T. Luo⁴², X. L. Luo^{1,a}, X. R. Lyu⁴¹, F. C. Ma²⁷, H. L. Ma¹, L. L. Ma³³, M. M. Ma¹, Q. M. Ma¹, T. Ma¹, X. N. Ma³⁰, X. Y. Ma^{1,a}, Y. M. Ma³³, F. E. Maas¹⁴, M. Maggiora^{49A,49C}, Y. J. Mao³¹, Z. P. Mao¹, S. Marcello^{49A,49C}, J. G. Messchendorp²⁵, G. Mezzadri^{21B}, J. Min^{1,a}, R. E. Mitchell¹⁹, X. H. Mo^{1,a}, Y. J. Mo⁶, C. Morales Morales¹⁴, N. Yu. Muchnoi^{9,e}, H. Muramatsu⁴³, P. Musiol⁴, Y. Nefedov²³, F. Nerling¹⁴, I. B. Nikolaev^{9,e}, Z. Ning^{1,a}, S. Nisar⁸, S. L. Niu^{1,a}, X. Y. Niu¹, S. L. Olsen³², Q. Ouyang^{1,a}, S. Pacetti^{20B}, Y. Pan^{46,a}, P. Patteri^{20A}, M. Pelizaeus⁴, H. P. Peng^{46,a}, K. Peters¹⁰, J. Pettersson⁵⁰, J. L. Ping⁵¹, R. G. Ping¹, R. Poling⁴³, V. Prasad¹, H. R. Qi², M. Qi²⁹, S. Qian^{1,a}, C. F. Qiao⁴¹, L. Q. Qin³³, N. Qin⁵¹, X. S. Qin¹, Z. H. Qin^{1,a}, J. F. Qiu¹, K. H. Rashid⁴⁸, C. F. Redmer²², M. Ripka²², G. Rong¹, Ch. Rosner¹⁴, X. D. Ruan¹², A. Sarantsev^{23,f}, M. Savri^{21B}, C. Schmier⁴, K. Schoenning⁵⁰, S. Schumann²², W. Shan³¹, M. Shao^{46,a}, C. P. Shen², P. X. Shen³⁰, X. Y. Shen¹, H. Y. Sheng¹, M. Shi¹, W. M. Song¹, X. Y. Song¹, S. Sosio^{49A,49C}, S. Spataro^{49A,49C}, G. X. Sun¹, J. F. Sun¹⁵, S. S. Sun¹, X. H. Sun¹, Y. J. Sun^{46,a}, Y. Z. Sun¹, Z. J. Sun^{1,a}, Z. T. Sun¹⁹, C. J. Tang³⁶, X. Tang¹, I. Tapan^{40C}, E. H. Thorndike⁴⁴, M. Tiemens²⁵, I. Uman^{40D}, G. S. Varner⁴², B. Wang³⁰, B. L. Wang⁴¹, D. Wang³¹, D. Y. Wang³¹, K. Wang^{1,a}, L. L. Wang¹, L. S. Wang¹, M. Wang³³, P. Wang¹, P. L. Wang¹, S. G. Wang³¹, W. Wang^{1,a}, W. P. Wang^{46,a}, X. F. Wang³⁹, Y. Wang³⁷, Y. D. Wang¹⁴, Y. F. Wang^{1,a}, Y. Q. Wang²², Z. Wang^{1,a}, Z. G. Wang^{1,a}, Z. H. Wang^{46,a}, Z. Y. Wang¹, Z. Y. Wang¹, T. Weber²², D. H. Wei¹¹, J. B. Wei³¹, P. Weidenkaff²², S. P. Wen¹, U. Wiedner⁴, M. Wolke⁵⁰, L. H. Wu¹, L. J. Wu¹, Z. Wu^{1,a}, L. Xia^{46,a}, L. G. Xia³⁹, Y. Xia¹⁸, D. Xiao¹, H. Xiao⁴⁷, Z. J. Xiao²⁸, Y. G. Xie^{1,a}, Q. L. Xiu^{1,a}, G. F. Xu¹, J. J. Xu¹, L. Xu¹, Q. J. Xu¹³, Q. N. Xu⁴¹, X. P. Xu³⁷, L. Yan^{49A,49C}, W. B. Yan^{46,a}, W. C. Yan^{46,a}, Y. H. Yan¹⁸, H. J. Yang³⁴, H. X. Yang¹, L. Yang⁵¹, Y. X. Yang¹¹, M. Ye^{1,a}, M. H. Ye⁷, J. H. Yin¹, B. X. Yu^{1,a}, C. X. Yu³⁰, J. S. Yu²⁶, C. Z. Yuan¹, W. L. Yuan²⁹, Y. Yuan¹, A. Yuncu^{40B,b}, A. A. Zafar⁴⁸, A. Zallo^{20A}, Y. Zeng¹⁸, Z. Zeng^{46,a}, B. X. Zhang¹, B. Y. Zhang^{1,a}, C. Zhang²⁹, C. C. Zhang¹, D. H. Zhang¹, H. H. Zhang³⁸, H. Y. Zhang^{1,a}, J. Zhang¹, J. J. Zhang¹, J. L. Zhang¹, J. Q. Zhang¹, J. W. Zhang^{1,a}, J. Y. Zhang¹, J. Z. Zhang¹, K. Zhang¹, L. Zhang¹, S. Q. Zhang³⁰, X. Y. Zhang³³, Y. Zhang¹, Y. H. Zhang^{1,a}, Y. N. Zhang⁴¹, Y. T. Zhang^{46,a}, Yu Zhang⁴¹, Z. H. Zhang⁶, Z. P. Zhang⁴⁶, Z. Y. Zhang⁵¹, G. Zhao¹, J. W. Zhao^{1,a}, J. Y. Zhao¹, J. Z. Zhao^{1,a}, Lei Zhao^{46,a}, Ling Zhao¹, M. G. Zhao³⁰, Q. Zhao¹, Q. W. Zhao¹, S. J. Zhao⁵³, T. C. Zhao¹, Y. B. Zhao^{1,a}, Z. G. Zhao^{46,a}, A. Zhemchugov^{23,c}, B. Zheng⁴⁷, J. P. Zheng^{1,a}, W. J. Zheng³³, Y. H. Zheng⁴¹, B. Zhong²⁸, L. Zhou^{1,a}, X. Zhou⁵¹, X. K. Zhou^{46,a}, X. R. Zhou^{46,a}, X. Y. Zhou¹, K. Zhu¹, K. J. Zhu^{1,a}, S. Zhu¹, S. H. Zhu⁴⁵,

X. L. Zhu³⁹, Y. C. Zhu^{46,a}, Y. S. Zhu¹, Z. A. Zhu¹, J. Zhuang^{1,a}, L. Zotti^{49A,49C}, B. S. Zou¹, J. H. Zou¹

(BESIII Collaboration)

- ¹ *Institute of High Energy Physics, Beijing 100049, People's Republic of China*
- ² *Beihang University, Beijing 100191, People's Republic of China*
- ³ *Beijing Institute of Petrochemical Technology, Beijing 102617, People's Republic of China*
- ⁴ *Bochum Ruhr-University, D-44780 Bochum, Germany*
- ⁵ *Carnegie Mellon University, Pittsburgh, Pennsylvania 15213, USA*
- ⁶ *Central China Normal University, Wuhan 430079, People's Republic of China*
- ⁷ *China Center of Advanced Science and Technology, Beijing 100190, People's Republic of China*
- ⁸ *COMSATS Institute of Information Technology, Lahore, Defence Road, Off Raiwind Road, 54000 Lahore, Pakistan*
- ⁹ *G.I. Budker Institute of Nuclear Physics SB RAS (BINP), Novosibirsk 630090, Russia*
- ¹⁰ *GSI Helmholtzcentre for Heavy Ion Research GmbH, D-64291 Darmstadt, Germany*
- ¹¹ *Guangxi Normal University, Guilin 541004, People's Republic of China*
- ¹² *GuangXi University, Nanning 530004, People's Republic of China*
- ¹³ *Hangzhou Normal University, Hangzhou 310036, People's Republic of China*
- ¹⁴ *Helmholtz Institute Mainz, Johann-Joachim-Becher-Weg 45, D-55099 Mainz, Germany*
- ¹⁵ *Henan Normal University, Xinxiang 453007, People's Republic of China*
- ¹⁶ *Henan University of Science and Technology, Luoyang 471003, People's Republic of China*
- ¹⁷ *Huangshan College, Huangshan 245000, People's Republic of China*
- ¹⁸ *Hunan University, Changsha 410082, People's Republic of China*
- ¹⁹ *Indiana University, Bloomington, Indiana 47405, USA*
- ²⁰ *(A)INFN Laboratori Nazionali di Frascati, I-00044, Frascati, Italy; (B)INFN and University of Perugia, I-06100, Perugia, Italy*
- ²¹ *(A)INFN Sezione di Ferrara, I-44122, Ferrara, Italy; (B)University of Ferrara, I-44122, Ferrara, Italy*
- ²² *Johannes Gutenberg University of Mainz, Johann-Joachim-Becher-Weg 45, D-55099 Mainz, Germany*
- ²³ *Joint Institute for Nuclear Research, 141980 Dubna, Moscow region, Russia*
- ²⁴ *Justus-Liebig-Universitaet Giessen, II. Physikalisches Institut, Heinrich-Buff-Ring 16, D-35392 Giessen, Germany*
- ²⁵ *KVI-CART, University of Groningen, NL-9747 AA Groningen, The Netherlands*
- ²⁶ *Lanzhou University, Lanzhou 730000, People's Republic of China*
- ²⁷ *Liaoning University, Shenyang 110036, People's Republic of China*
- ²⁸ *Nanjing Normal University, Nanjing 210023, People's Republic of China*
- ²⁹ *Nanjing University, Nanjing 210093, People's Republic of China*
- ³⁰ *Nankai University, Tianjin 300071, People's Republic of China*
- ³¹ *Peking University, Beijing 100871, People's Republic of China*
- ³² *Seoul National University, Seoul, 151-747 Korea*
- ³³ *Shandong University, Jinan 250100, People's Republic of China*
- ³⁴ *Shanghai Jiao Tong University, Shanghai 200240, People's Republic of China*
- ³⁵ *Shanxi University, Taiyuan 030006, People's Republic of China*
- ³⁶ *Sichuan University, Chengdu 610064, People's Republic of China*
- ³⁷ *Soochow University, Suzhou 215006, People's Republic of China*
- ³⁸ *Sun Yat-Sen University, Guangzhou 510275, People's Republic of China*
- ³⁹ *Tsinghua University, Beijing 100084, People's Republic of China*
- ⁴⁰ *(A)Ankara University, 06100 Tandogan, Ankara, Turkey; (B)Istanbul Bilgi University, 34060 Eyup, Istanbul, Turkey; (C)Uludag University, 16059 Bursa, Turkey; (D)Near East University, Nicosia, North Cyprus, Mersin 10, Turkey*
- ⁴¹ *University of Chinese Academy of Sciences, Beijing 100049, People's Republic of China*
- ⁴² *University of Hawaii, Honolulu, Hawaii 96822, USA*
- ⁴³ *University of Minnesota, Minneapolis, Minnesota 55455, USA*
- ⁴⁴ *University of Rochester, Rochester, New York 14627, USA*
- ⁴⁵ *University of Science and Technology Liaoning, Anshan 114051, People's Republic of China*
- ⁴⁶ *University of Science and Technology of China, Hefei 230026, People's Republic of China*
- ⁴⁷ *University of South China, Hengyang 421001, People's Republic of China*
- ⁴⁸ *University of the Punjab, Lahore-54590, Pakistan*

⁴⁹ (A) *University of Turin, I-10125, Turin, Italy; (B) University of Eastern Piedmont, I-15121, Alessandria, Italy; (C) INFN, I-10125, Turin, Italy*
⁵⁰ *Uppsala University, Box 516, SE-75120 Uppsala, Sweden*

⁵¹ *Wuhan University, Wuhan 430072, People's Republic of China*

⁵² *Zhejiang University, Hangzhou 310027, People's Republic of China*

⁵³ *Zhengzhou University, Zhengzhou 450001, People's Republic of China*

^a *Also at State Key Laboratory of Particle Detection and Electronics, Beijing 100049, Hefei 230026, People's Republic of China*

^b *Also at Bogazici University, 34342 Istanbul, Turkey*

^c *Also at the Moscow Institute of Physics and Technology, Moscow 141700, Russia*

^d *Also at the Functional Electronics Laboratory, Tomsk State University, Tomsk, 634050, Russia*

^e *Also at the Novosibirsk State University, Novosibirsk, 630090, Russia*

^f *Also at the NRC "Kurchatov Institute", PNPI, 188300, Gatchina, Russia*

^g *Also at University of Texas at Dallas, Richardson, Texas 75083, USA*

^h *Also at Istanbul Arel University, 34295 Istanbul, Turkey*

(Dated: October 22, 2016)

The process $e^+e^- \rightarrow \eta' J/\psi$ is observed for the first time with a statistical significance of 8.6σ at center-of-mass energy $\sqrt{s} = 4.226$ GeV and 7.3σ at $\sqrt{s} = 4.258$ GeV using data samples collected with the BESIII detector. The Born cross sections are measured to be $(3.7 \pm 0.7 \pm 0.3)$ and $(3.9 \pm 0.8 \pm 0.3)$ pb at $\sqrt{s} = 4.226$ and 4.258 GeV, respectively, where the first errors are statistical and the second systematic. Upper limits at the 90% confidence level of the Born cross sections are also reported at other 12 energy points.

PACS numbers: 13.25.Gv, 13.66.Bc, 14.40.Pq, 14.40.Rt

I. INTRODUCTION

The region of center-of-mass (c.m.) energies above the open charm threshold is of great interest due to the richness of charmonium states, whose properties are not well understood. Until now, the vector states $\psi(3770)$, $\psi(4040)$, $\psi(4160)$, and $\psi(4415)$ are well established experimentally in the hadronic cross section in e^+e^- annihilation [1] and match very well with the calculation in the quark model of charmonium [2]. By exploiting the initial state radiation (ISR) process, the B-factories BaBar and Belle discovered several new charmonium-like vector states, the $Y(4260)$, $Y(4360)$, and $Y(4660)$, via their decays into the hidden-charm final states $\pi^+\pi^- J/\psi$ or $\pi^+\pi^-\psi(3686)$ [3–7], while there are no corresponding structures observed in the cross sections to open-charm or inclusive hadronic final states. In contrast, the decay of the excited ψ states into the above two hidden-charm final states has not been observed to date. The overpopulation of the vector states between 4.0 and 4.7 GeV/ c^2 triggered many discussions about the nature of these states and the possible discovery of new kinds of hadrons [8].

Besides the $\pi^+\pi^-$ hadronic transitions, information on other hadronic transitions will provide further insight on the internal structure of these charmonium and charmonium-like states. CLEO-c, BESIII, and Belle measured the cross section of $e^+e^- \rightarrow \eta J/\psi$ [9–11], which has significant contribution from the $\psi(4040)$ and $\psi(4160)$ decays and is different from the predic-

tion in Ref. [12], which is obtained by considering virtual charmed meson loops. Treating η and η' with the Light-Cone approach and J/ψ with non-relativistic QCD, and together with the contribution of the resonance decays, the authors of Ref. [13] can reproduce the measured $e^+e^- \rightarrow \eta J/\psi$ line shape and predict the production cross section of the analogous process $e^+e^- \rightarrow \eta' J/\psi$ at c.m. energies \sqrt{s} from 4.3 to 5.3 GeV.

To check the theoretical predictions [13] and to search for potential $\eta' J/\psi$ transitions from charmonium and charmonium-like states, we measure the process $e^+e^- \rightarrow \eta' J/\psi$ with the data taken at BESIII. The CLEO-c experiment searched for this process with data at c.m. energies \sqrt{s} from 3.970 to 4.260 GeV and did not observe the signal [9].

In this paper, we report measurements of the Born cross section for $e^+e^- \rightarrow \eta' J/\psi$ at 14 energy points \sqrt{s} from 4.189 to 4.600 GeV [14]. The data samples are collected with the BESIII detector [15] operating at the BEPCII storage ring. The total integrated luminosity is about 4.5 fb^{-1} , which is measured using large angle Bhabha events with an uncertainty of 1% [16]. In the analysis, the J/ψ is reconstructed through its decays into lepton pairs $J/\psi \rightarrow \ell^+\ell^-$ ($\ell = e$ or μ), while the η' is reconstructed in two decay channels, $\eta' \rightarrow \eta\pi^+\pi^-$ (with $\eta \rightarrow \gamma\gamma$) and $\eta' \rightarrow \gamma\pi^+\pi^-$.

II. DETECTOR AND MONTE CARLO SIMULATION

The BESIII [15] detector is a general purpose spectrometer at the BEPCII accelerator [17] for studies of hadron spectroscopy and physics in the τ -charm energy region [18]. The design peak luminosity of the double-ring e^+e^- collider, BEPCII, is $10^{33} \text{ cm}^{-2}\text{s}^{-1}$ at $\sqrt{s} = 3.77 \text{ GeV}$ with a beam current of 0.93 A.

The BESIII detector with a geometrical acceptance of 93% of 4π consists of the following main components: 1) a main drift chamber (MDC) equipped with 6796 signal wires and 21884 field wires arranged in a small cell configuration with 43 layers working in a gas mixture of He (40%) and C_3H_8 (60%). The single wire resolution on average is $135 \mu\text{m}$, and the momentum resolution for charged particles in a 1 T magnetic field is 0.5% at 1 GeV; 2) a time-of-flight system (TOF) for particle identification made of 176 pieces of 5 cm thick, 2.4 m long plastic scintillators arranged as a cylinder with two layers for the barrel, and 96 fan-shaped, 5 cm thick, plastic scintillators for two end-caps. The time resolution is 80 ps in the barrel, and 110 ps in the end-caps, corresponding to a K/π separation at 2σ level up to about 1.0 GeV; 3) an electromagnetic calorimeter (EMC) made of 6240 CsI(Tl) crystals arranged in a cylindrical shape, complemented by two endcaps. The energy resolution is 2.5% in the barrel and 5% in the endcaps at 1.0 GeV; the position resolution is 6 mm in the barrel and 9 mm in the endcaps at 1.0 GeV. The time resolution of the EMC is 50 ns. 4) a muon chamber system (MUC) in the iron flux return yoke of the solenoid, made of resistive plate chambers (RPC) arranged in 9 layers in the barrel and 8 layers in the endcaps, with a resolution of 2 cm.

In order to optimize the selection criteria, determine the detection efficiency and estimate potential background contributions, Monte Carlo (MC) simulated data samples are generated using a GEANT4-based [19] software, which takes into account the detector geometry and material description, the detector response and signal digitization, as well as the records of the detector running conditions and performances. The signal MC samples of $e^+e^- \rightarrow \eta' J/\psi$ are generated at each c.m. energy point assuming that the Born cross section follows an incoherent sum of a Breit-Wigner (BW) function for the $\psi(4160)$ resonance and a polynomial term for the continuum production. For the background study, inclusive MC samples including the $Y(4260)$ decays, ISR production of the vector charmonium states, continuum production of hadrons and QED processes are generated with KKMC [20, 21] at $\sqrt{s} = 4.258, 4.416, \text{ and } 4.600 \text{ GeV}$. For the inclusive MC samples, the main known decay modes are generated with EVTGEN [21], and the remaining events associated with charmonium decays are generated with the LUNDCHARM [22] model, while continuum hadronic events are generated with PYTHIA [23].

III. EVENT SELECTION AND STUDY OF BACKGROUND SHAPE

The candidate events of $e^+e^- \rightarrow \eta' J/\psi$ are required to have four charged tracks with zero net charge. All charged tracks are required to be well reconstructed in the MDC with good helix fit quality and to satisfy $|\cos\theta| < 0.93$, where θ is the polar angle of the track in the laboratory frame. The charged tracks are required to originate from the interaction region with $R_{xy} < 1.0 \text{ cm}$ and $|R_z| < 10.0 \text{ cm}$, where R_{xy} and R_z are the distances of closest approach of the charged track to the interaction point perpendicular to and along the beam direction, respectively. A charged track with momentum less than 0.8 GeV is assigned to be a pion candidate, while a track with momentum larger than 1.0 GeV is assigned to be a lepton candidate. Electron and muon separation is carried out by the ratio E/p of energy deposited in the EMC and momentum measured in the MDC. For electron candidates, we require an E/p ratio larger than 0.8, while for muon candidates, the E/p ratio is required to be less than 0.4.

Photon candidates are reconstructed from showers in the EMC crystals. The minimum energy of photon is required to be 25 MeV in the barrel ($|\cos\theta| < 0.80$) or 50 MeV in the end-cap ($0.86 < |\cos\theta| < 0.92$). To eliminate showers produced by charged particles, the angle between the shower and the nearest charged track is required to be greater than 20 degrees. EMC cluster timing is further required to be between 0 and 700 ns to suppress electronic noise and energy deposits unrelated to the event. The number of good photon candidates is required to be at least 1 for $\eta' \rightarrow \gamma\pi^+\pi^-$ and at least 2 for $\eta' \rightarrow \eta\pi^+\pi^-$.

For $\eta' \rightarrow \gamma\pi^+\pi^-$, a four-constraint (4C) kinematic fit is performed on the four selected charged tracks ($\pi^+\pi^-\pi^+\pi^-$ or $\pi^+\pi^-\mu^+\mu^-$) and one good photon candidate to improve the momentum and energy resolutions of the final-state particles and to reduce the potential background. If there is more than one photon in an event, the one resulting in the minimum χ_{4C}^2 of the kinematic fit is retained for further study. The χ_{4C}^2 is required to be less than 40. For $\eta' \rightarrow \eta\pi^+\pi^-$, a five-constraint (5C) kinematic fit is performed on the four charged tracks ($\pi^+\pi^-\pi^+\pi^-$ or $\pi^+\pi^-\mu^+\mu^-$) and two good photon candidates, with the additional constraint on the invariant mass of $\gamma\gamma$ to be equal to the η nominal mass [1]. For events with more than two photons, the combination with the minimum χ_{5C}^2 is chosen. The χ_{5C}^2 is required to be less than 40.

Besides the requirements described above, the following selection criteria are applied to select the signal. For the decay channel $\eta' \rightarrow \gamma\pi^+\pi^-$, in order to eliminate the backgrounds from ISR processes with $\psi(3686)$ in the final state or from the process $e^+e^- \rightarrow \pi^+\pi^- J/\psi$ with Final State Radiation (FSR) from the leptons, the invariant mass of $\pi^+\pi^- J/\psi$ ($M(\pi^+\pi^- J/\psi)$)

and the invariant mass of the system recoiling against $\pi^+\pi^-$ ($M^{\text{recoil}}(\pi^+\pi^-)$) are required to be out of the regions $3.65 < M(\pi^+\pi^-J/\psi) < 3.71 \text{ GeV}/c^2$ and $3.05 < M^{\text{recoil}}(\pi^+\pi^-) < 3.15 \text{ GeV}/c^2$, respectively. For the decay channel $\eta' \rightarrow \eta\pi^+\pi^-$, the corresponding distributions are required to be out of the regions $3.67 < M(\pi^+\pi^-J/\psi) < 3.71 \text{ GeV}/c^2$ and $3.65 < M^{\text{recoil}}(\pi^+\pi^-) < 3.69 \text{ GeV}/c^2$ to eliminate the background reactions $e^+e^- \rightarrow \eta\psi(3686) \rightarrow \eta\pi^+\pi^-J/\psi$ and $e^+e^- \rightarrow \pi^+\pi^-\psi(3686) \rightarrow \pi^+\pi^-\eta J/\psi$, respectively.

After applying the above selection criteria, Fig. 1 shows the invariant mass distribution of $\ell^+\ell^-$ for events with the invariant mass of $\gamma(\eta)\pi^+\pi^-$ within the η' signal and sideband regions for the data samples at $\sqrt{s} = 4.226$ and 4.258 GeV . Here, the η' signal region is defined as $(0.94, 0.98) \text{ GeV}/c^2$, while η' sideband regions are $(0.90, 0.94) \text{ GeV}/c^2$ and $(0.98, 1.02) \text{ GeV}/c^2$. The J/ψ signals are observed clearly at both energy points. According to the MC study, the small peaking background visible in the sideband distribution around the J/ψ mass comes from $e^+e^- \rightarrow \gamma_{\text{ISR}}\pi^+\pi^-J/\psi$, which does not produce peaking background in the distribution of $M(\gamma\pi^+\pi^-)$. The mass window requirement $3.07 < M(\ell^+\ell^-) < 3.13 \text{ GeV}/c^2$ is used to select J/ψ signal for further study. After imposing all these selection criteria, the background contribution is investigated with the inclusive MC samples. The dominant backgrounds are found to be those with the same final states as the signal events but without η' or J/ψ intermediate states, and can not be eliminated completely.

IV. SIGNAL DETERMINATION

After applying all of the above selection criteria except for the η' mass window requirement, the invariant mass distributions of $\gamma\pi^+\pi^-$ and $\eta\pi^+\pi^-$ for $J/\psi \rightarrow e^+e^-$ and $J/\psi \rightarrow \mu^+\mu^-$ individually as well as the combination of four channels are shown in Fig. 2 and Fig. 3 for the data at $\sqrt{s} = 4.226$ and 4.258 GeV , respectively. The η' is observed clearly in the combined distribution. The background is a flat distribution in the $\gamma\pi^+\pi^-$ invariant mass; this is verified by studying the corresponding distributions of the events in the J/ψ sideband region and of the MC samples. The invariant mass distribution of the $\eta\pi^+\pi^-$ channel is essentially background free.

To determine the signal yields, a simultaneous fit to the invariant mass of $\gamma(\eta)\pi^+\pi^-$ with an unbinned maximum likelihood method is performed for the four different channels. The total signal yield, denoted as N^{tot} , is a free parameter in the fit. The signal yields for the individual decay modes are constrained by assuming the same production cross section for $e^+e^- \rightarrow \eta'J/\psi$ and are determined to be $N^{\text{tot}} \times \mathcal{B}(\eta') \times \mathcal{B}(J/\psi) \times \epsilon$, where $\mathcal{B}(\eta')$ and $\mathcal{B}(J/\psi)$ are the decay branching fractions of η' and J/ψ , respectively, and ϵ is the corresponding detection efficiency. The η' signal is described by a MC simu-

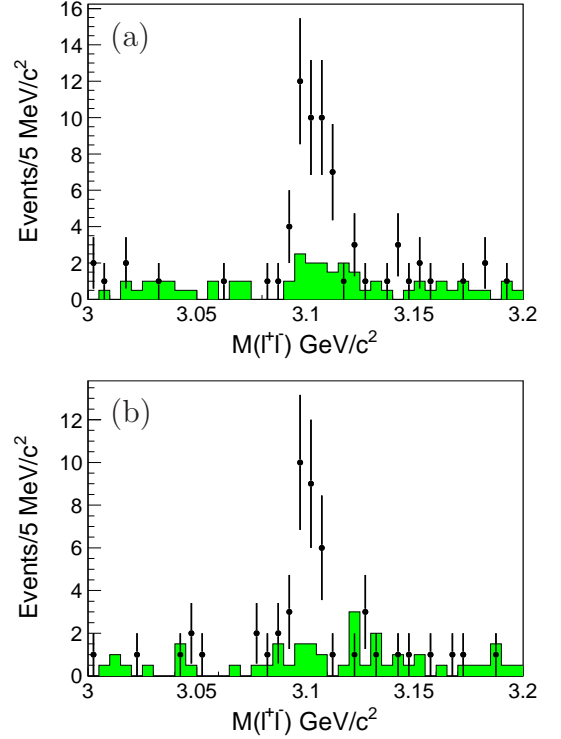


FIG. 1: The $M(\ell^+\ell^-)$ distribution of data summed over the four channels ($\eta' \rightarrow \eta\pi^+\pi^-/\gamma\pi^+\pi^-$ and $J/\psi \rightarrow e^+e^-/\mu^+\mu^-$) at (a) $\sqrt{s} = 4.226 \text{ GeV}$ and (b) $\sqrt{s} = 4.258 \text{ GeV}$. The dots with error bars and the (green) shaded histograms represent events within η' signal and sideband regions, respectively.

lated shape convolved with a Gaussian function to take into account the mass resolution difference between data and the MC simulation; the parameters of the Gaussian function are free but constrained to be the same for the different channels. The background is described with a linear function, and its normalization factors are allowed to vary in different channels.

Projections of the mode-by-mode and combined fit results at $\sqrt{s} = 4.226 \text{ GeV}$ are shown in Fig. 2. The χ^2/ndf for the combined result is 0.9, where sparsely populated bins are combined so that there are at least seven counts per bin in the χ^2 calculation and ndf is the number of degrees of freedom. The fit yields $N^{\text{obs}} = 36.5 \pm 6.9$, and the statistical significance of the η' signal is determined to be 8.6σ by comparing the log-likelihood values with and without η' signal included in the fit and taking the change of the number of free parameters into account. A similar fit process is performed for the data at $\sqrt{s} = 4.258 \text{ GeV}$, and corresponding results are shown in Fig. 3. The χ^2/ndf for the combined result is 0.94, the fit yields $N^{\text{obs}} = 30.0 \pm 6.2$ and the statistical significance of the η' signal is 7.3σ .

The same event selection criteria are applied to the data samples taken at the other 12 energy points.

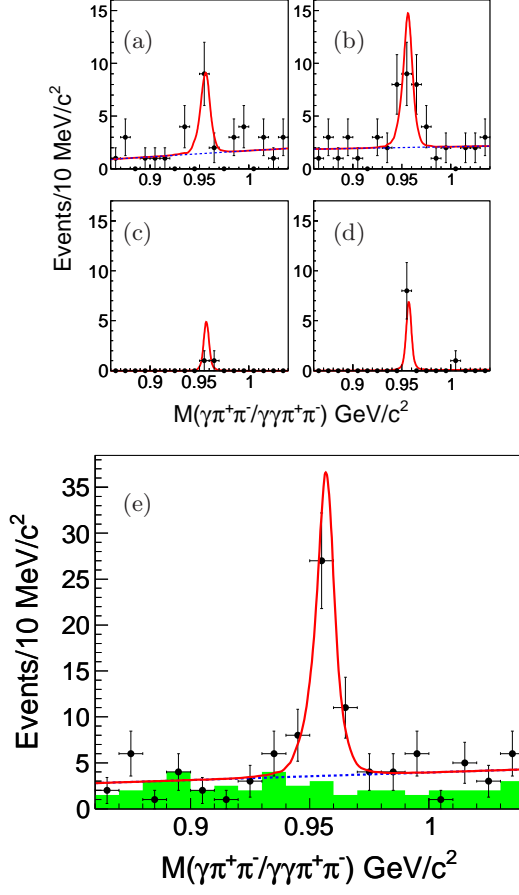


FIG. 2: Simultaneous fit to the $M(\gamma\pi^+\pi^-/\gamma\gamma\pi^+\pi^-)$ spectra at $\sqrt{s} = 4.226$ GeV. (a) for $\eta' \rightarrow \gamma\pi^+\pi^-$ and $J/\psi \rightarrow e^+e^-$, (b) for $\eta' \rightarrow \gamma\pi^+\pi^-$ and $J/\psi \rightarrow \mu^+\mu^-$, (c) for $\eta' \rightarrow \eta\pi^+\pi^-$ and $J/\psi \rightarrow e^+e^-$, (d) for $\eta' \rightarrow \eta\pi^+\pi^-$ and $J/\psi \rightarrow \mu^+\mu^-$. (e) shows the combined result. The dots with error bars and the (green) shaded histograms represent events from data within the J/ψ signal and sideband regions, respectively. The solid lines show the fit results, while the dashed lines represent the background.

Figure 4 depicts the scatter plot of $M(\ell^+\ell^-)$ versus $M(\gamma\pi^+\pi^-/\eta\pi^+\pi^-)$ and the projections of $M(\ell^+\ell^-)$ and $M(\gamma\pi^+\pi^-/\eta\pi^+\pi^-)$ including all 12 energy points. We can see a cluster of events in the signal region, although no significant $\eta'J/\psi$ signal is observed at any individual energy point. As a consequence, upper limits on the number of signal events at the 90% confidence level (C.L.) are set using a Bayesian method [24] at every individual energy point. By fitting the $M(\gamma\pi^+\pi^-/\eta\pi^+\pi^-)$ distribution with fixed values for the signal yield, we obtain a scan of the likelihood as a function of the number of signal events. The upper limit is determined by finding the number of signal events below which lies 90% of the area under the likelihood distribution. The results are listed in Table I.

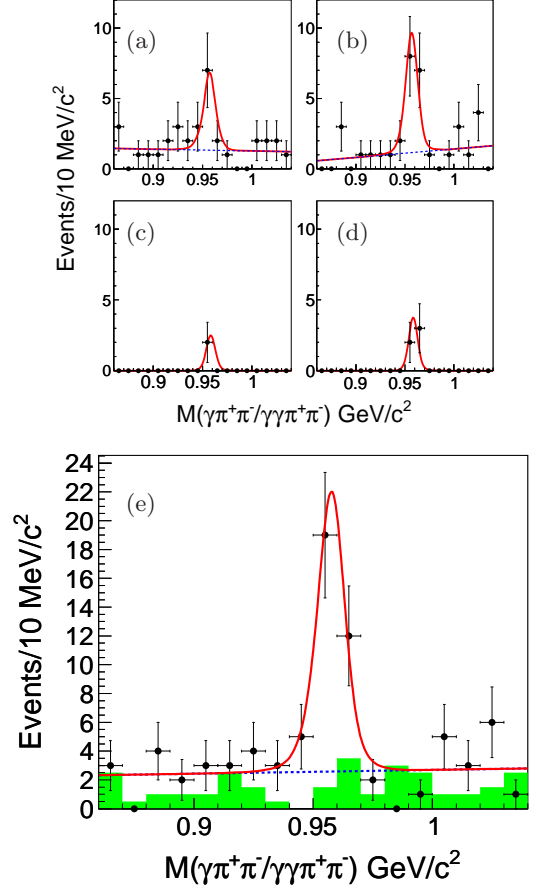


FIG. 3: Simultaneous fit to the $M(\gamma\pi^+\pi^-/\gamma\gamma\pi^+\pi^-)$ spectra at $\sqrt{s} = 4.258$ GeV. (a) for $\eta' \rightarrow \gamma\pi^+\pi^-$ and $J/\psi \rightarrow e^+e^-$, (b) for $\eta' \rightarrow \gamma\pi^+\pi^-$ and $J/\psi \rightarrow \mu^+\mu^-$, (c) for $\eta' \rightarrow \eta\pi^+\pi^-$ and $J/\psi \rightarrow e^+e^-$, (d) for $\eta' \rightarrow \eta\pi^+\pi^-$ and $J/\psi \rightarrow \mu^+\mu^-$. (e) shows the combined result. The dots with error bars and the (green) shaded histograms represent events from data within the J/ψ signal and sideband regions, respectively. The solid lines show the fit results, while the dashed lines represent the background.

V. CROSS SECTION RESULTS

The Born cross section is calculated with

$$\sigma^B = \frac{N^{\text{obs}}}{L_{\text{int}} \cdot (1 + \delta) \cdot |1 + \Pi|^2 \cdot \sum_{i=1}^4 \epsilon_i \mathcal{B}_i}, \quad (1)$$

where L_{int} is the integrated luminosity, ϵ_i is selection efficiency for the i th channel estimated from the MC simulation, \mathcal{B}_i is the product branching fraction of the intermediate states for the i th channel taken from the Particle Data Group [1], $|1 + \Pi|^2$ is the vacuum polarization factor [25] and $(1 + \delta)$ is the radiative correction factor, which is defined as

$$1 + \delta = \frac{\int_0^1 \sigma(s(1-x))F(x,s)dx}{\sigma(s)}. \quad (2)$$

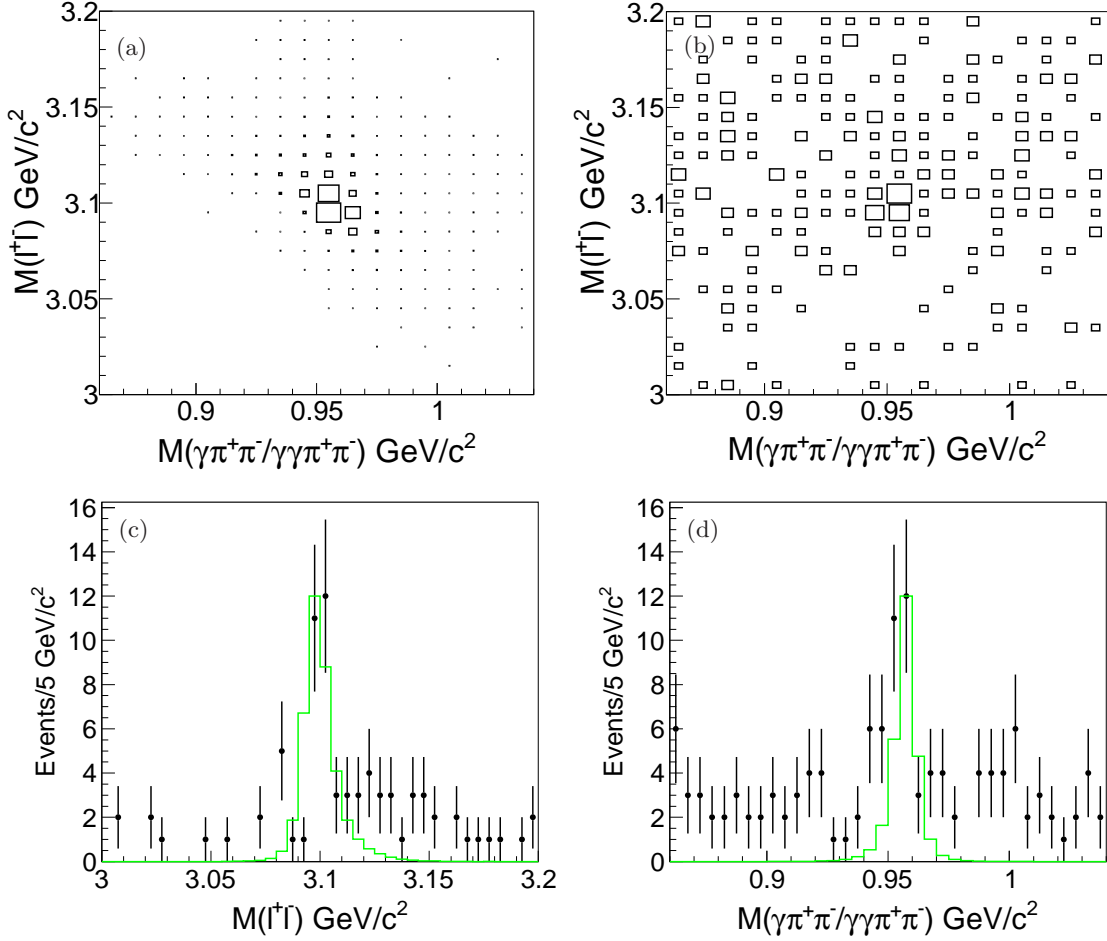


FIG. 4: The distributions for the data samples taken at $\sqrt{s} = 4.189, 4.208, 4.217, 4.242, 4.308, 4.358, 4.387, 4.416, 4.467, 4.527, 4.575$, and 4.600 GeV, (a) the scatter plot of $M(\ell^+\ell^-)$ versus $M(\gamma\pi^+\pi^-/\gamma\gamma\pi^+\pi^-)$ for the MC simulation; (b) the corresponding scatter plot for the data; (c) the projection of $M(\ell^+\ell^-)$, and (d) the projection of $M(\gamma\pi^+\pi^-/\gamma\gamma\pi^+\pi^-)$, in which points with error bars are data and histograms are signal MC simulation.

The radiative correction changes the total cross section, and emission of additional photons affects the efficiency of selection. Here, x is the ratio between radiative photon's energy and the center of mass energy, $F(x, s)$ is the radiator function, which is obtained from a QED calculation [26] with an accuracy of 0.1%, and $\sigma(s)$ is the line shape of the cross section for $e^+e^- \rightarrow \eta' J/\psi$, which is described by a constant-width BW function with the parameters of the $\psi(4160)$ plus a polynomial function.

All the numbers used in the cross section calculation are summarized in Table I. The Born cross section is measured to be (3.7 ± 0.7) pb at 4.226 GeV and (3.9 ± 0.8) pb at 4.258 GeV, where the errors are statistical. The Born cross sections and upper limits at the other energy points are also shown in Table I. In the upper limit determination, a conservative result with a factor $1/(1 - \sigma)$ is included to take into account the effect of the total systematic uncertainty, σ , which is described in the next section in detail.

Figure 5 shows the measured Born cross sections for $e^+e^- \rightarrow \eta' J/\psi$ over the energy region studied in this work. Assuming that the $\eta' J/\psi$ signals come from the $\psi(4160)$ decay, the cross section is fitted with a constant-width relativistic BW function, i.e.,

$$\sigma(m) = |\mathcal{A}_{\psi(4160)}(m) \cdot \sqrt{\Phi(m)/\Phi(M)}|^2, \quad (3)$$

where $\mathcal{A}_{\psi(4160)}(m)$ represents the contribution of $\psi(4160) \rightarrow \eta' J/\psi$ and $\Phi(m)$ is the 2-body phase space factor. Here, $\mathcal{A}_{\psi(4160)}(m)$ is written as below:

$$\mathcal{A}_{\psi(4160)}(m) = \frac{\sqrt{12\pi\Gamma_{ee}\Gamma_{\text{tot}}\mathcal{B}(\psi(4160) \rightarrow \eta' J/\psi)}}{m^2 - M^2 + iM\Gamma_{\text{tot}}}, \quad (4)$$

where the resonant parameters (the mass M , the total width Γ_{tot} and the electron partial width Γ_{ee}) of the $\psi(4160)$ and the branching ratio for $\psi(4160) \rightarrow \eta' J/\psi$ are taken from PDG [1] and fixed in the fit. The χ^2/ndf is 0.9, which means the measurement supports our assumption. The second resonance, $\psi(4415)$ [1], is also

TABLE I: Summary of the values used to calculate the Born cross section of $e^+e^- \rightarrow \eta' J/\psi$. The upper limits are at the 90% C.L.

\sqrt{s} (GeV)	N^{obs}	L_{int} (pb $^{-1}$)	$1+\delta$	$\sum \epsilon_i \mathcal{B}_i$ (10^{-2})	$ 1+\Pi ^2$	σ^{B} (pb)
4.189	3.8 ± 2.3 (< 8.7)	43.1	0.857	1.01	1.056	$9.7 \pm 5.8 \pm 0.6$ (< 24)
4.208	2.6 ± 3.2 (< 13.3)	54.6	0.885	1.04	1.057	$4.9 \pm 6.1 \pm 0.4$ (< 27)
4.217	1.0 ± 1.7 (< 6.2)	54.1	0.902	1.00	1.057	$1.9 \pm 3.3 \pm 0.2$ (< 13)
4.226	36.5 ± 6.9	1047.3	0.919	0.98	1.056	$3.7 \pm 0.7 \pm 0.3$
4.242	0.8 ± 1.4 (< 5.3)	55.6	0.945	0.95	1.056	$1.5 \pm 2.7 \pm 0.2$ (< 11)
4.258	30.0 ± 6.2	825.7	0.969	0.91	1.054	$3.9 \pm 0.8 \pm 0.3$
4.308	2.2 ± 1.5 (< 5.9)	44.9	1.036	0.81	1.052	$5.6 \pm 3.8 \pm 0.3$ (< 16)
4.358	3.0 ± 2.3 (< 7.9)	539.8	1.114	0.77	1.051	$0.6 \pm 0.5 \pm 0.1$ (< 1.7)
4.387	2.1 ± 2.1 (< 8.3)	55.2	1.162	0.73	1.051	$4.3 \pm 4.3 \pm 0.3$ (< 18)
4.416	10.8 ± 4.1 (< 15.9)	1028.9	1.191	0.71	1.053	$1.2 \pm 0.5 \pm 0.1$ (< 2.0)
4.467	5.9 ± 4.1 (< 14.8)	109.9	1.161	0.72	1.055	$6.1 \pm 4.2 \pm 0.5$ (< 17)
4.527	1.4 ± 1.3 (< 5.3)	110.0	1.002	0.81	1.055	$1.5 \pm 1.4 \pm 0.1$ (< 6.1)
4.575	0.0 ± 1.7 (< 9.0)	47.7	0.907	0.90	1.055	$0.0 \pm 4.2 \pm 0.4$ (< 24)
4.600	1.2 ± 2.3 (< 7.9)	566.9	0.880	0.92	1.055	$0.3 \pm 0.5 \pm 0.1$ (< 2.1)

added in the fit; the statistical significance is determined to be 2.6σ by comparing the two $-2\ln(L)$ values and taking the change of ndf into account. It indicates that the contribution of $\psi(4415)$ is not significant.

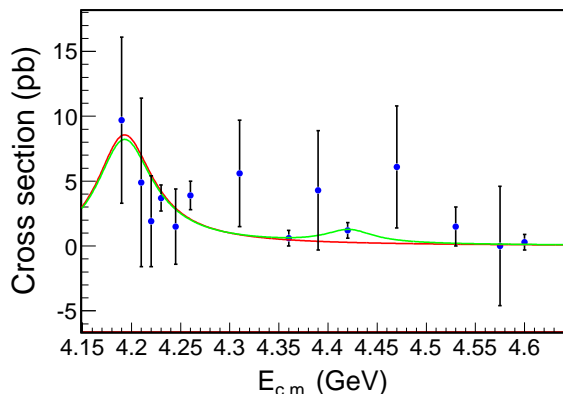


FIG. 5: Fit to the Born cross section $\sigma(e^+e^- \rightarrow \eta' J/\psi)$ with a $\psi(4160)$ resonance (red curve), or a combination of $\psi(4160)$ and $\psi(4415)$ resonances (green curve). The uncertainties are statistical only.

VI. SYSTEMATIC UNCERTAINTIES

Several sources of systematic uncertainties are considered in the measurement of the Born cross section, including the integrated luminosity measurement, background shape, fitting range, ISR correction factor, photon detection, tracking efficiency, kinematic fit, lepton pair mass resolution, and the branching fractions of intermediate states decay.

(a) The uncertainty from integrated luminosity measurement using large angle Bhabha ($e^+e^- \rightarrow e^+e^-$) scattering is estimated to be 1.0% [16].

(b) The systematic uncertainty due to the background shape is estimated by varying the background shape from a linear function to a second order Chebyshev polynomial. The difference in the signal yields is taken as the systematic uncertainty.

(c) The systematic uncertainty due to the fit range is estimated by varying the fit range from $[0.86, 1.04]$ GeV/ c^2 to $[0.87, 1.05]$ GeV/ c^2 or $[0.85, 1.03]$ GeV/ c^2 . The largest change in the signal yields is taken as the systematic uncertainty.

Since the relative signal yields for each individual decay mode i is constrained by the weight factor $\epsilon_i \mathcal{B}_i / \sum_{i=1}^4 \epsilon_i \mathcal{B}_i$ in the fit procedure, the uncertainties due to ϵ_i or \mathcal{B}_i affect not only $\epsilon_i \mathcal{B}_i$ but also N^{obs} . Taking both terms into account, we change the values of ϵ_i or \mathcal{B}_i , then refit the data. The change of the measured cross section is taken as the systematic uncertainty. The following systematic uncertainties are estimated by this method except for the tracking efficiency. Because the four decay channels have the same, fully correlated, uncertainty on the tracking efficiency, this uncertainty will not affect the fit result. Most of these uncertainties are energy independent, except that associated with ISR correction. We use the uncertainties determined with data at the high-statistics energy point $\sqrt{s} = 4.226$ GeV as the systematic uncertainties for all the samples.

(d) The ISR correction factors are obtained by a QED calculation using the cross section measured by this analysis, which is parameterized by a BW function for $\psi(4160)$ plus a polynomial function. The ISR correction factors are calculated iteratively until they become stable. To estimate the uncertainty due to the ISR correction factor, the measured cross section is also parameterized by a BW function or a polynomial function. The largest discrepancy between the results with alternative assumption and the nominal value is taken as the systematic uncertainty.

(e) The uncertainty due to photon reconstruction effi-

ciency is 1.0% per photon [27]. Therefore, we vary the values of ϵ_i up or down by $1\% \times N_\gamma$ and refit the data, where N_γ is the number of photons in the final state. The maximum change of the measured cross section is taken as the systematic uncertainty.

(f) The discrepancy of tracking efficiency between the MC simulation and the data is estimated to be 1.0% per charged track from a study of $e^+e^- \rightarrow \pi^+\pi^-J/\psi$ and $e^+e^- \rightarrow 2(\pi^+\pi^-)$. There are 4 charged tracks in the candidate events, 4.0% is adopted as the changed value for ϵ_i , so the total uncertainty in the final results is 4.0%.

(g) The mass resolution discrepancy between the MC simulation and the data will introduce an uncertainty when we apply a mass window requirement on the invariant mass distribution of the lepton pairs. This uncertainty is estimated using the control sample $e^+e^- \rightarrow \gamma_{\text{ISR}}\psi(3686) \rightarrow \gamma_{\text{ISR}}\pi^+\pi^-J/\psi$ with $J/\psi \rightarrow e^+e^-$ or $\mu^+\mu^-$. The same J/ψ mass window [3.07, 3.13] GeV/ c^2 is required for both the data and the MC sample, and the discrepancy in efficiency between the MC simulation and the data is $(1.0 \pm 1.1)\%$ and $(2.9 \pm 1.6)\%$ for $J/\psi \rightarrow e^+e^-$ and $\mu^+\mu^-$, respectively. After refitting the data, the large change on the measured cross section with respect to the nominal value is taken as the systematic uncertainty.

(h) The uncertainty associated with the kinematic fit arises from the inconsistency of track helix parameters between the data and the MC simulation. Therefore, the three track parameters ϕ_0 , κ , and $\tan\lambda$ are corrected in the signal MC samples. The correction factors are obtained by comparing their pull distributions in a control sample between data and MC simulation [28]. The difference of the detection efficiency between the samples with and without the helix correction affects the weight factors. The data is refitted and the resulting difference on the Born cross section with respect to the nominal value is taken as the systematic uncertainty.

(i) The branching fractions of $J/\psi \rightarrow e^+e^-/\mu^+\mu^-$, $\eta' \rightarrow \gamma\pi^+\pi^-/\eta\pi^+\pi^-$, and $\eta \rightarrow \gamma\gamma$ are changed independently. The sum in quadrature of all individual uncertainties on the Born cross section is taken as the systematic uncertainty.

(j) Final state radiation affects both the lepton pair invariant mass distribution and the efficiency of the kinematic fit; its systematic uncertainty is taken into account. The uncertainties related with the requirements to veto backgrounds are negligibly small, and the uncertainties from other sources such as the E/p ratio requirement for electron and muon separation, the vacuum polarization and c.m. energy measurement are estimated to be less than 1% and are neglected in this analysis.

The sources of systematic uncertainty and their contributions are summarized in Table II. The total systematic uncertainty is the sum in quadrature of all individual uncertainties.

VII. SUMMARY

In summary, the process $e^+e^- \rightarrow \eta'J/\psi$ is investigated using data samples collected with the BESIII detector at 14 c.m. energies from 4.189 to 4.600 GeV. Significant $e^+e^- \rightarrow \eta'J/\psi$ signals are observed at $\sqrt{s} = 4.226$ and 4.258 GeV for the first time, and the corresponding Born cross sections are measured to be $(3.7 \pm 0.7 \pm 0.3)$ and $(3.9 \pm 0.8 \pm 0.3)$ pb, respectively. The upper limits of Born cross sections at the 90% C.L. are set for the other 12 c.m. energy points where no significant signal is observed. The measured cross sections support the hypothesis that signal events of $\eta'J/\psi$ come from $\psi(4160)$ decays; the contribution of $\psi(4415)$ is not evident.

Compared with the Born cross section of $e^+e^- \rightarrow \eta J/\psi$ [11], the measured Born cross section of $e^+e^- \rightarrow \eta'J/\psi$ is much smaller, which is in contradiction to the calculation in Ref. [13]. There are two possible reasons contributing to this discrepancy. The cross section of $e^+e^- \rightarrow \eta'J/\psi$ is investigated at an order of $O(\alpha_s^4)$, therefore, higher order correction might need to be considered; additionally, the proportion of gluonic admixture in η' need to be further studied to make certain the contribution of a gluonium component on the results.

Acknowledgments

The BESIII collaboration thanks the staff of BEPCII and the IHEP computing center for their strong support. This work is supported in part by National Key Basic Research Program of China under Contract No. 2015CB856700; National Natural Science Foundation of China (NSFC) under Contracts Nos. 11125525, 11235011, 11322544, 11335008, 11425524; the Chinese Academy of Sciences (CAS) Large-Scale Scientific Facility Program; the CAS Center for Excellence in Particle Physics (CCEPP); the Collaborative Innovation Center for Particles and Interactions (CICPI); Joint Large-Scale Scientific Facility Funds of the NSFC and CAS under Contracts Nos. 11179007, U1232201, U1332201; CAS under Contracts Nos. KJCX2-YW-N29, KJCX2-YW-N45; 100 Talents Program of CAS; National 1000 Talents Program of China; INPAC and Shanghai Key Laboratory for Particle Physics and Cosmology; German Research Foundation DFG under Contract No. Collaborative Research Center CRC-1044; Istituto Nazionale di Fisica Nucleare, Italy; Koninklijke Nederlandse Akademie van Wetenschappen (KNAW) under Contract No. 530-4CDP03; Ministry of Development of Turkey under Contract No. DPT2006K-120470; Russian Foundation for Basic Research under Contract No. 14-07-91152; The Swedish Research Council; U. S. Department of Energy under Contracts Nos. DE-FG02-04ER41291, DE-FG02-05ER41374, DE-SC-0010504, de-sc0012069, DESC0010118; U.S. National

TABLE II: Summary of systematic uncertainties (%).

Source/ \sqrt{s} (GeV)	4.189	4.208	4.217	4.226	4.242	4.258	4.308	4.358	4.387	4.415	4.467	4.527	4.575	4.600
Luminosity measurement	1.0	1.0	1.0	1.0	1.0	1.0	1.0	1.0	1.0	1.0	1.0	1.0	1.0	1.0
Background shape	0.1	3.4	5.3	0.2	4.9	2.4	0.1	0.2	0.6	4.6	0.1	0.2	0.0	2.9
Fit range	0.4	4.1	2.7	2.2	0.7	2.2	0.3	5.1	0.2	7.7	6.1	1.2	0.0	3.5
ISR factor	3.0	1.2	3.0	4.0	4.4	1.1	2.5	2.1	2.9	1.7	1.5	2.9	6.0	2.1
Photon detection	1.4	1.4	1.4	1.4	1.4	1.4	1.4	1.4	1.4	1.4	1.4	1.4	1.4	1.4
Tracking efficiency	4.0	4.0	4.0	4.0	4.0	4.0	4.0	4.0	4.0	4.0	4.0	4.0	4.0	4.0
Kinematic fitting	1.1	1.1	1.1	1.1	1.1	1.1	1.1	1.1	1.1	1.1	1.1	1.1	1.1	1.1
Lepton pair mass resolution	2.2	2.2	2.2	2.2	2.2	2.2	2.2	2.2	2.2	2.2	2.2	2.2	2.2	2.2
Branching fraction	1.6	1.6	1.6	1.6	1.6	1.6	1.6	1.6	1.6	1.6	1.6	1.6	1.6	1.6
Total	6.1	7.6	8.5	7.0	8.5	6.3	5.8	7.6	6.0	10.5	8.2	6.1	8.0	7.3

Science Foundation; University of Groningen (RuG) and the Helmholtzzentrum fuer Schwerionenforschung GmbH (GSI), Darmstadt; WCU Program of National Research

Foundation of Korea under Contract No. R32-2008-000-10155-0.

-
- [1] K. A. Olive *et al.* [Particle Data Group], Chin. Phys. C **38**, 090001 (2014).
[2] T. Barnes, S. Godfrey, and E. S. Swanson, Phys. Rev. D **72**, 054026 (2005).
[3] B. Aubert *et al.* [BaBar Collaboration], Phys. Rev. Lett. **95**, 142001 (2005); J. P. Lees *et al.* [BABAR Collaboration], Phys. Rev. D **86**, 051102(R) (2012).
[4] B. Aubert *et al.* [BABAR Collaboration], Phys. Rev. Lett. **98**, 212001 (2007); J. P. Lees *et al.* [BABAR Collaboration], Phys. Rev. D **89**, 111103(R) (2014).
[5] C. Z. Yuan *et al.* [Belle Collaboration], Phys. Rev. Lett. **99**, 182004 (2007); Z. Q. Liu *et al.* [Belle Collaboration], Phys. Rev. Lett. **110**, 252002 (2013).
[6] X. L. Wang *et al.* [Belle Collaboration], Phys. Rev. Lett. **99**, 142002 (2007); G. Pakhlova *et al.* [Belle Collaboration], Phys. Rev. Lett. **111**, 172001 (2008); X. L. Wang *et al.* [Belle Collaboration], Phys. Rev. D **91**, no. 11, 112007 (2015).
[7] Q. He *et al.* [CLEO Collaboration], Phys. Rev. D **74**, 091104(R) (2006).
[8] For a recent review, see N. Brambilla *et al.*, Eur. Phys. J. C **71**, 1534 (2011).
[9] T. E. Coan *et al.* [CLEO Collaboration], Phys. Rev. Lett. **96**, 162003 (2006).
[10] X. L. Wang *et al.* [Belle Collaboration], Phys. Rev. D **87**, 051101 (2013).
[11] M. Ablikim *et al.* [BESIII Collaboration], Phys. Rev. D **86**, 071101 (2012); M. Ablikim *et al.* [BESIII Collaboration], Phys. Rev. D **91**, 112005 (2015).
[12] Q. Wang, X. -H. Liu and Q. Zhao, Phys. Rev. D **84**, 014007 (2011).
[13] C. F. Qiao, R. L. Zhu, Phys. Rev. D **89**, 074006 (2014).
[14] M. Ablikim *et al.* [BESIII Collaboration], Chin. Phys. C **40**, 063001 (2016).
[15] M. Ablikim *et al.* [BESIII Collaboration], Nucl. Instrum. Meth. A **614**, 345 (2010).
[16] M. Ablikim *et al.* [BESIII Collaboration], Chin. Phys. C **39**, 093001 (2015).
[17] J. Z. Bai *et al.* [BES Collaboration], Nucl. Instrum. Meth. A **458**, 627 (2001); **344**, 319 (1994).
[18] D. M. Asner *et al.*, Int. J. Mod. Phys. A **24**, S1 (2009).
[19] S. Agostinelli *et al.* [GEANT4 Collaboration], Nucl. Instrum. Meth. A **506**, 250 (2003).
[20] S. Jadach, B. F. L. Ward and Z. Was, Phys. Rev. D **63**, 113009 (2001).
[21] R. G. Ping, Chin. Phys. C **32**, 599 (2008); D. J. Lange, Nucl. Instrum. Meth. A **462**, 152 (2001).
[22] J. C. Chen, G. S. Huang, X. R. Qi, D. H. Zhang and Y. S. Zhu, Phys. Rev. D **62**, 034003 (2000).
[23] <http://home.thep.lu.se/~torbjorn/Pythia.html>
[24] J. Conrad *et al.*, Phys. Rev. D **67**, 012002 (2003).
[25] S. Actis *et al.* [Working Group on Radiative Corrections and Monte Carlo Generators for Low Energies Collaboration], Eur. Phys. J. C **66**, 585 (2010).
[26] E. A. Kuraev and V. S. Fadin, Sov. J. Nucl. Phys. **41**, 466 (1985) [Yad. Fiz. **41**, 733 (1985)].
[27] M. Ablikim *et al.* [BESIII Collaboration], Phys. Rev. D **81**, 052005 (2010).
[28] M. Ablikim *et al.* [BESIII Collaboration], Phys. Rev. D **87**, 012002 (2013).